Overlap-Stiffened Panels for Optimized Buckling Performance Under Minimum Steering Radius Constraints

Raphael Ummels[a,*], Saullo G. P. Castro[a,*]

[a]Faculty of Aerospace Engineering, Delft University of Technology, Delft, The Netherlands

ARTICLE INFO

Keywords:
Overlap-stiffened panel
Design
Optimization
Variable stiffness
Variable angle tow
Tow overlap
Buckling
Manufacturing constraint
Minimum steering radius

ABSTRACT

Recent research on variable stiffness laminates have shown both numerically and experimentally that further improvement on the buckling behaviour is possible by incorporating overlaps that result in variable thickness profiles, with the thickness non-linearly coupled with the local steering angle. We present the concept of overlap-stiffened panels, developing a design method that allows for incorporating higher-stiffness regions into individual plies of a variable-angle tow (VAT) laminate, taking advantage of the non-linear coupling between the tow steering angles and the local thickness. The proposed method naturally copes with minimum steering radius constraints of different manufacturing processes, and the present study considers two tow steering processes: automated fiber placement (AFP) and continuous tow shearing (CTS). The minimum radius constraint is satisfied by connecting two transition regions of thickness specified on each ply by means of circular fiber tow arcs, of which the radius of curvature always exceed the minimum manufacturing constraint. Each individual ply exploring the overlap-stiffened design is described using 5 design variables. Laminates made up of these overlap-stiffened plies are optimized for a maximum volume-normalized buckling performance under bi-axial compression, measured through FEM, by a genetic algorithm and benchmarked against a straight fiber panel optimized for the same load case. The conclusion can be drawn that both AFP and CTS overlap-stiffened VAT panels can at least achieve the double of the volume-normalized buckling performance of an optimized straight fiber panel, demonstrating the potential of the proposed design method.

1. Introduction

Novel automated manufacturing techniques have the capability to steer the fibers of each layer towards curvilinear paths, producing varying fiber orientation that reflects in variable stiffness, which ultimately enables a higher tailoring potential of composite materials. This opens even more the development and application of advanced lightweight composite structural designs. For instance, substantial improvements in buckling loads were achieved by varying the laminate stiffness in the direction perpendicular to the applied load due to a redistribution of the primary loads from the center section of the panel to the simply supported sides of the panel [1, 2, 3].

The variable angle tows utilized in the present study can be realized during manufacturing mainly by means of bending and shearing [4]. When the tows are sheared, as in the continuous tow shearing process [5], the tow width measured perpendicularly to the tow path changes according to $w_{tow}\cos\theta$; where w_{tow} is the nominal tow thickness and θ the tow steering angle. Note that when shearing occurs the tow thickness must change due to conservation of mass [6].

Variable angle tows can also be achieved by means of in-plane bending [1, 7], keeping the tow width constant if measured perpendicularly to the tow path, which creates residual in-plane stresses on the tows to accommodate the variable-angle [4]. Ultimately, this residual in-plane stresses will determine the minimum radius of curvature achievable in VAT designs [7]. In automated fiber placement (AFP), it is customary to avoid thickness variation during fiber steering by means of cut-and-restart [3]. In the present study, advanced composite designs are explored by allowing thickness build-up created by the nonlinear steering-thickness coupling inherent of the CTS process, and also achievable using an overlap-based design in the AFP process.

An approximate relationship between the local thickness of an individual ply and the local fiber angle plies where tow overlaps are allowed, was derived by Castro et al. [6], whereby a ply can thus be designed for a specific thickness distribution, by tailoring the fiber directions within the ply to create that thickness distribution. Using this, stiffener-like structures could essentially be woven into the plies of a composite laminate structure during manufacturing, ostensibly resulting in a higher buckling failure load of the final product.

The present study sets out to complete two main goals. First, develop a design method that can reliably generate the aforementioned overlap-stiffened plies by taking advantage of the nonlinear steering-thickness coupling. These plies should be physically possible to manufacture without irregularities, by having the minimum radius of tow curvature constrained according to the selected manufacturing process. Moreover, the design should preferably be described with as little variables as possible.

Second, develop a method for testing and optimizing such overlap-stiffened plies for a given structural performance. In the present study, the linear buckling performance is investigated for panels manufactured by means of AFP and a CTS, and compared with the performance of a well-known opti-

*Corresponding Authors
r.ummels@student.tudelft.nl (R. Ummels);
S.G.P.Castro@tudelft.nl (S.G.P. Castro)
ORCID(s): 0000-0001-9711-0991 (S.G.P. Castro)

mized straight-fiber laminate plate from Haftka [8].

By fulfilling these two goals, the authors can prove the concept for the new overlap-stiffened design method herein proposed, opening up a whole new world of new design possibilities.

2. Proposed design concept

The production of variable-angle tow (VAT) composite laminated structures via automated fiber placement (AFP) is achieved by means of robots that are capable of laying tapes or tows of pre-impregnated (prepreg) fibers along predefined computerized paths [2]. More modern AFP processes make use of thermoplastic prepregs, whereby the tapes are heated by a laser source [7]. By laying the tows next to one another, full plies covering the region of interest are created, and the process is repeated until the desired full VAT laminate is deposited. An arbitrary tow within a VAT ply is depicted in Figure 1, where θ represents the local fiber angle between the local tow path and the x-axis of the plate domain.

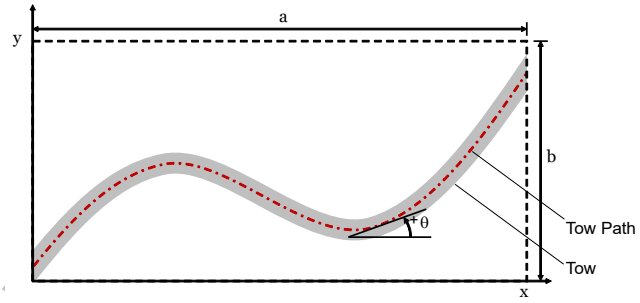

Figure 1: Arbitrary tow path of one tow within a ply. Theta is counter clockwise positive, originating from the positive x axis.

2.1. Thickness and fiber angle distribution

Uninterrupted curved tows cannot be laid neatly next to each other to produce a ply without creating gaps or overlaps [2, 3], or without using alternative production methods of variable angle tow such as continuous tow shearing (CTS) [5]. In general, one would like to avoid irregularities like gaps or localized thickness increases due to overlaps. However, the thickness increase created by overlaps in fiber reinforced composite laminates can actually be used to significantly increase the load carrying capacity and buckling performance [9].

Blom et al. [3] derived an approximate formula for a relationship between the width of a tow and the effective width as a function of the local tow angle was proposed. Based on this relationship, Castro et al. [6] derived Equation 1, which gives an approximate relationship between the effective local ply thickness, $t_{(x,y)}$ and the local fiber angle, $\theta_{(x,y)}$ within an overlap ply, based on conservation of mass. In the present study, t_p represents the nominal thickness of a tow and $t(x, y)$ the local varying thickness.

$$t(x, y) \approx \frac{t_p}{\cos(\theta(x, y))} \tag{1}$$

Based on Eq. 1, note that a local fiber steering angle of 60° would thus result in an approximate doubling of the effective local ply thickness.

The origin of this effective thickness increase is illustrated in Figure 2 and Figure 3. In Figure 2 adjacent tows follow a path from 0° to 70° and back again from left to right. More and more regions of doubled and tripled ply thickness created by tow overlaps crop up as the local fiber angle increases. When these localized overlaps are spread out, or smeared out, over the surrounding area, it creates the thickness distribution shown in Figure 3. This smeared out thickness distribution was the basis for Equation 1. Lander and Castro [10, 11] compared the differences in modelling the exact thickness distribution vs. the smeared thickness distribution, demonstrating the good correlation and equivalence in buckling response of the smeared approach compared to a discrete representation of the overlaps.

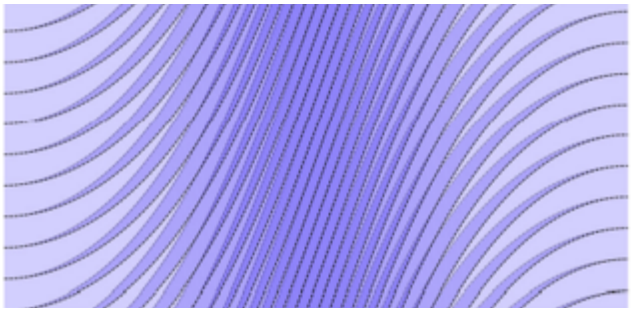

Figure 2: The exact thickness distribution created by overlapping adjacent tows through curvature. [6]

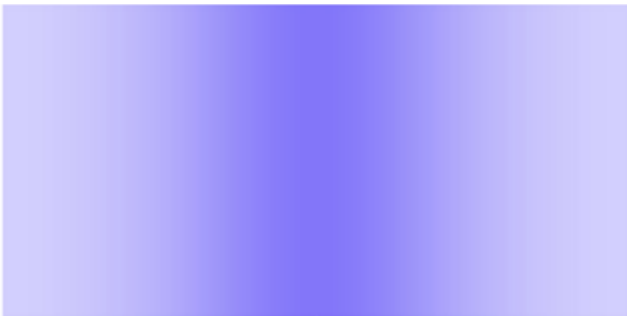

Figure 3: The approximate smeared out thickness distribution created by overlapping adjacent tows through curvature. [6]

2.2. Overlap-stiffened plies and laminates

The relationship given in Equation 1 gives rise to the idea that one can design VAT overlap plies and laminates for a given thickness distribution by tailoring the fiber angle distribution to create the wanted thickness distribution.

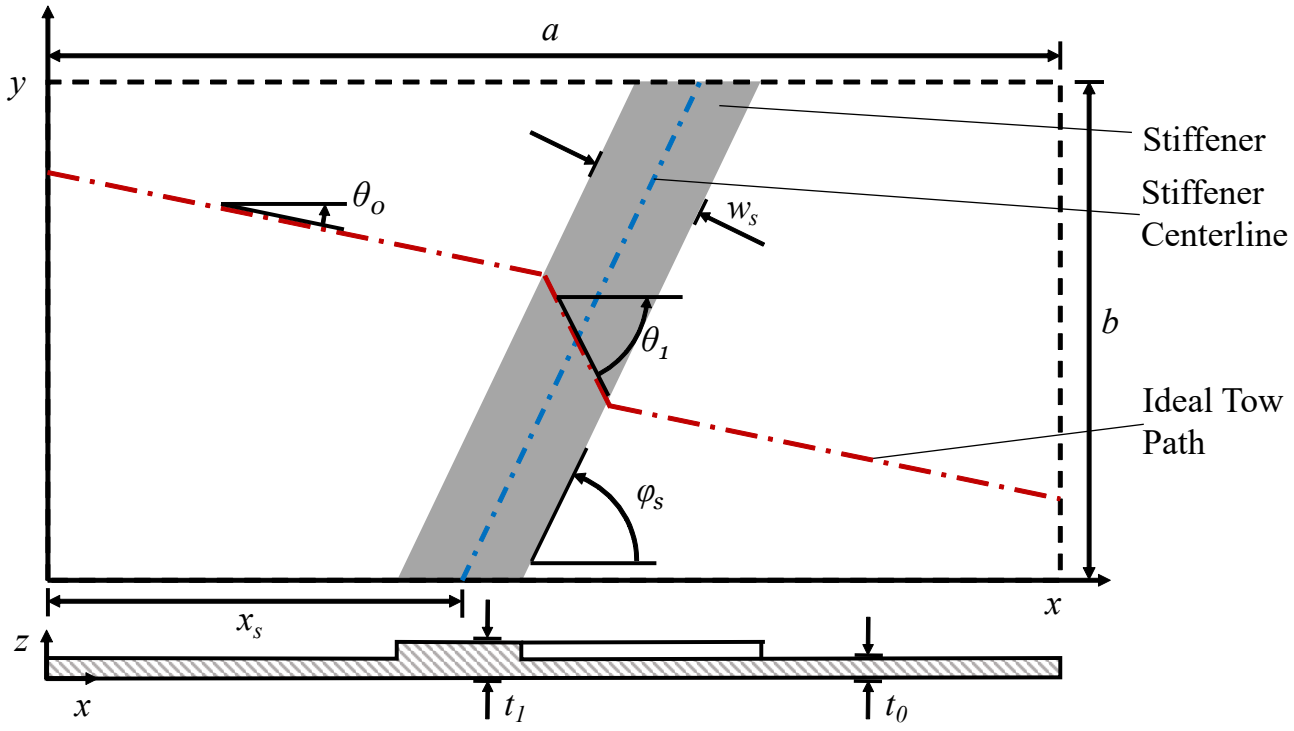

Figure 4: The geometric description of an ideal stiffener within an overlap-stiffened ply.

Stiffener-like thickness distributions could essentially be woven into the plies of the laminates during production.

The geometry of an idealized arbitrary overlap-stiffener within a ply is pictured in Figure 4. The darker grey region is the region of increased thickness, which mimics a stiffener. The fiber angle is set to θ_1 in the dark grey region, with the rest of the ply having a fiber angle of θ_0. If a tow laying machine were to follow these angles it would lay paths like the example tow path given in red. The tow paths follow the direction of the specified fiber angle distribution from edge to edge. Angles θ_1 and θ_0 respectively translate to t_1 and t_0 using Equation 1. Here $\theta_1 > \theta_0$, and thus $t_1 > t_0$.

The width of the stiffener is given by w_s. The angle of the stiffener with respect to the x-axis is defined as ϕ_s. Finally, the position of the stiffener along the horizontal axis of the ply is given by x_s. A ply has a length of a in x-direction, and a width of b in the y-direction. The thickness of the ply is measured in z-direction.

As a result, an idealized overlap-stiffened ply within an a by b laminate made with a tow thickness of t_p can be described by a vector, $\boldsymbol{P}$, of only 5 variables, given in Equation 2.

$$\boldsymbol{P_{i,n}} = [\theta_{0_{i,n}}, \theta_{1_{i,n}}, w_{s_{i,n}}, \phi_{s_{i,n}}, x_{s_{i,n}}] \tag{2}$$

A full laminate of n plies can then be described by a vector of plies, $\boldsymbol{L}$, as per Equation 3.

$$\boldsymbol{L_i} = [\boldsymbol{P_{i,1}}, \boldsymbol{P_{i,2}}, \dots, \boldsymbol{P_{i,n}}] \tag{3}$$

The previously mentioned geometric variables have a number of constraints. First off, to ensure that plies can reliably be automatically generated without having the change of the tow path entering the stiffener and never leaving again, ϕ_s is always set to be of opposite sign compared to the sign of θ_0, and θ_1. It is theoretically possible to have them be all the same sign in certain ranges of angle combinations, but the current constraint ensures physically possible angle distributions with minimal added complexity to the ply generation algorithm in all cases.

The next constraint is given in Equation 4. A ϕ_s larger than 45° or smaller than -45° combined with a 0° fiber angle along the x-axis would result in the overlap effect being flipped, with the tows now actually diverging away from one another if they enter the stiffener, thus resulting in gaps instead of overlaps.

$$|\phi_s| \geq 45° \tag{4}$$

Stiffeners with $-45° < \phi_s < 45°$ can still be created through a rotation trick with the ply generation algorithm. If ϕ_s corresponds to this range it is first converted to $\phi_{s,a}$ using Equation 5.

$$\begin{aligned} \phi_{s,a} &= 90 + \phi_s \qquad \phi_s \leq 0 \\ \phi_{s,a} &= -90 + \phi_s \qquad \phi_s > 0 \end{aligned} \tag{5}$$

All of the other ply variables are fed into the ply generation algorithm as normal together with $\phi_{s,a}$, but with the width a and the height b values swapped. This results in the

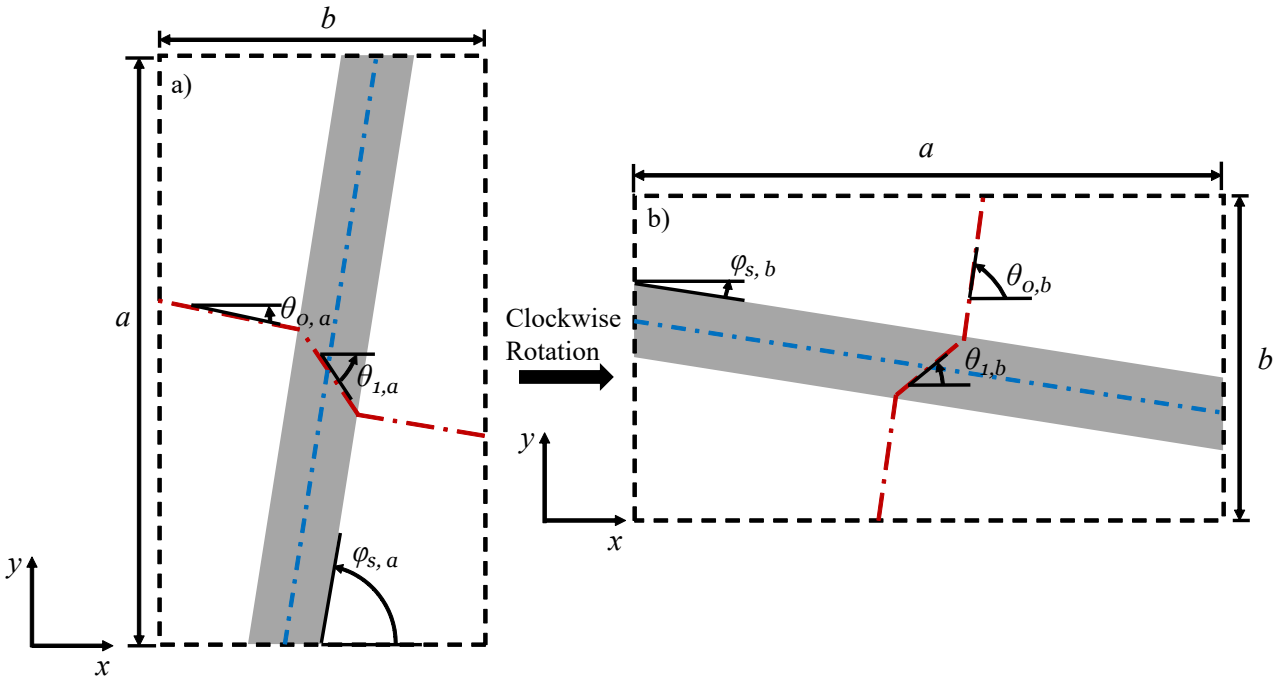

Figure 5: a) Starting orientation of a ply with -45° < ϕ_s < 45°. Note that the width is denoted by b, and the height by a. b) Orientation of the ply with -45° < ϕ_s < 45° after 90° clockwise rotation to align with the other plies in the axb laminate. Note that the general fiber direction is in the y direction for such a ply, not the x direction.

ply shown in Figure 5–a), where $\theta_{0,a} = \theta_0$ and $\theta_{1,a} = \theta_1$. The local thickness values are subsequently derived from the values of $\theta_{0,a}$ and $\theta_{1,a}$.

If the ply is now rotated by 90°in the clockwise direction, moving from a) to b) in Figure 5, $\phi_{s,b}$ will equal ϕ_s, and the tow path will obey all intersection constraints. The translation from θ_a to θ_b is given in Equation 6.

$$\begin{aligned} \theta_b &= = 90 + \phi_s \qquad \theta_a \leq 0 \\ \theta_b &= = -90 + \phi_s \qquad \theta_a > 0 \end{aligned} \tag{6}$$

It should be reiterated that the local thickness values are calculated with $\theta_{0,a}$ and $\theta_{1,a}$ not $\theta_{0,b}$ and $\theta_{1,b}$.

Furthermore, there are constraints on θ_0 and θ_1. For θ_0, the constraint is according to Equation 7, which was required to limit the amount of overlap outside of the designated stiffener area; θ_1 is constrained by Equation 8, which was required to avoid irregularities caused by having tows overlaps of more than 3 times the tow thickness, as the overlap height will start to reduce the accuracy of Equation 1. In addition, the plate model also starts to become a poor approximation of the shallow shell for steering angles over 60°, as discussed by Groh and Weaver [12] .

Additionally, θ_0 is also constrained to be smaller than θ_1 in Equation 9 to consider only designs that actually produce a desired region with higher thickness.

$$|\theta_0| \leq 30° \tag{7}$$

$$|\theta_1| \leq 60° \tag{8}$$

$$\theta_1 > \theta_0 \tag{9}$$

Putting all of the previously mentioned constraints together leads to the following design space for the assembly of the ply vectors:

$$\begin{aligned}
& w_s \in (0, 0.2) && [m] \\
& x_s \in [0, a] && [m] \\
& \phi_s \in [-90, 90] && [°] \\
& \textbf{if} \quad \phi_s \in [0, 90] : \\
& \quad \theta_1 \in [-60, 0] && [°] \\
& \quad \textbf{if} \quad \theta_1 > -30 : \\
& \quad\quad \theta_0 \in (\theta_1, 0] && [°] \\
& \quad \textbf{else} : \\
& \quad\quad \theta_0 \in [-30, 0] && [°] \\
& \textbf{if} \quad \phi_s \in [-90, 0) : \\
& \quad \theta_1 \in [0, 90] && [°] \\
& \quad \textbf{if} \quad \theta_1 < 30 : \\
& \quad\quad \theta_0 \in [0, \theta_1) && [°] \\
& \quad \textbf{else} : \\
& \quad\quad \theta_0 \in [0, 30] && [°] \\
& \boldsymbol{P} = [\theta_0, \theta_1, w_s, \phi_s, x_s]
\end{aligned}$$

2.3. Minimum radius of curvature constraint

The minimum radius of curvature that the tow paths can achieve is dictated by the manufacturing method. The main

method considered in this paper is automated fiber placement (AFP), which has a relatively large minimum radius of curvature requirement. This is because the fibers are essentially bent into a curved shape, which causes buckling and wrinkling of the fibres on the inside of the curved tow, where compressive stresses develop.

A secondary method that is considered is continuous tow shearing (CTS) [5]. This production method curves the fibers through shear, avoiding residual stresses on the fibres and therefore avoiding tow wrinkling. Much smaller radii of curvature can be achieved as a result.

The stiffened ply as defined in Figure 4 cannot be produced with current AFP processes without compromising the fibers significantly. Looking at the idealized stiffened ply in a) of Figure 6, one can see that at the edges of the stiffener the tow path angle transfers instantaneously from θ_0 to θ_1 and vice versa. This turn effectively has a radius of curvature of 0 mm. Laminates produced with AFP typically have to have paths with a minimum radius of curvature, R_0, of at least 400 mm for state-of-the-art thermoplastic tows heated with a laser source [7] and 500 mm for thermoset tows [5].

For the AFP design, the minimum radius of curvature will be set to 450 mm for the purposes of this paper. For the CTS design, the minimum radius can be reduced to 50 mm [5].

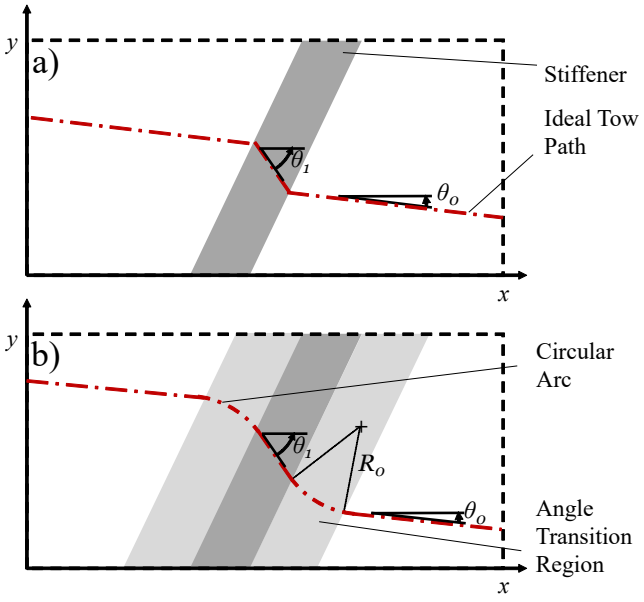

Figure 6: a): Tow path of idealized stiffener thickness distribution. b): Tow path of stiffener thickness distribution obeying the minimum radius of curvature manufacturing constraint.

Making sure all possible ply geometries which can be generated within the previously mentioned design space satisfy the minimum radius of curvature constraint might seems like a very complex problem at first. Fortunately, there is a simple yet powerful solution which satisfies this constraint for all plies within the design space. The tow paths can be defined such that they follow the exact circular arcs with radius R_0 required to go from θ_0 to θ_1 when entering the stiffener, and to go from θ_1 to θ_0 when exiting the stiffener on the other side. A tow path connected by these circular arcs is illustrated in b) of Figure 6.

These circular arcs are straightforwardly implemented in the ply generation algorithm used in the present study, which consists of three steps:

Step 1: The idealized stiffener geometry is assigned on a 101 by 101 reference grid with width a and height b. This is illustrated in Figure 7 a). The grid used in the image is 41 x 41 to make it easier to see individual grid spaces. A grid size of 101 by 101 ensures that the transitions are relatively smooth, and that there are no gaps due to large discretization steps;

Step 2: A circular arc grid stencil is generated based on the θ_0 and θ_1 values of the current ply, and the size of the grid rectangles in the reference grid. The stencil used in Figure 7 can be found in Figure 8. The angle values the grid spaces in the stencil are assigned are the angles the fibers need to follow the arc shape of the stencil at the location of those grid spaces.;

Step 3: The algorithm cycles through the reference grid, identifies the entry and exit edges of the stiffener, and pastes the arc stencil along the edges of the stiffener in the correct orientation, depending on whether its an entry or an exit edge. This results in the angle distribution grid seen in Figure 7 b), which can be converted to a thickness distribution using Equation 1. These three steps are performed for every ply within a laminate.

The idealized stiffener is now accompanied by an 'angle transition region', where the angle value is transitioning from θ_0 to θ_1 or vice versa. This in turn leads to a thickness transition region, as the local fiber angle dictates the local thickness. This can be seen in the three ply plots in Figure 9.

3. Fast buckling evaluation of variable stiffness plates

The design concept herein proposed will be explored using a robust optimization scheme driven genetic algorithm, explained in the next section. Given the high number of individuals evaluated in the genetic algorithm scheme, a fast constraint evaluation is preferred. For linear buckling of composite plates, fast analytical [13, 14, 15]. Semi-analytical methods are extremely recommended when the structural matrices can be analytically integrated, because these methods are able to approximate the continuum with less degrees-of-freedom when compared to other lower-order interpolation methods such as finite elements. However, when numerical integration is needed, the non-local support of the degrees-of-freedom involved in semi-analytical modelling requires integrands of the size of the entire structural matrices to be evaluated per integration point, making the integration process slower [16, 17]. Even tough the integration becomes slower, the reduced number of degrees-of-freedom to discretize the continuum might compensate [10].

The complexity of the stiffness variation of the present designs motivated the authors to use an alternative method

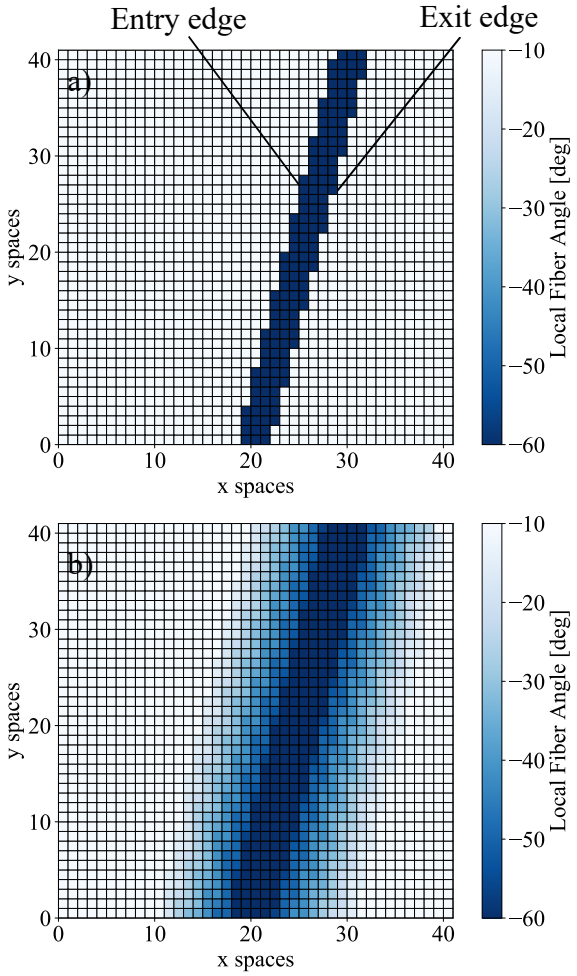

Figure 7: a) Initial idealized stiffener assigned on the reference grid. b) The stiffener after the algorithm has applied the circular arc stencil to all edges. The reference grid is set to 41x41 to make the gridlines visible in this example.

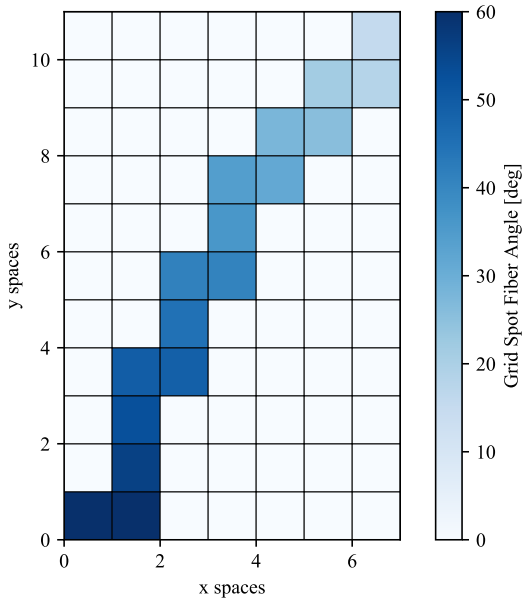

Figure 8: Stencil used in Figure 7 to attach to the entry and exit edges to create the circular arc transition region.

to semi-analytical approaches, that would allow a high-order approximation of the continuum while keeping the local support of the degrees-of-freedom, as detailed next.

3.1. Bogner-Fox-Schmit finite element

The Bogner-Fox-Schmit (BFS) finite element [18] is a classical C1 contiguous confirming plate element known as one of the most accurate rectangular finite elements for thin-walled shells, as stated by Zienkiewicz & Taylor [19, p. 153]. Recently, this element has been enriched by Castro and Jansen [20] to allow for fast post-buckling analysis using the Koiter method. The field approximation for the BFS is obtained by taking tensor products of cubic Hermite splines. With only 4 nodes per element, the standard BFS element approximates the out-of-plane displacements using 3^{rd}–order polynomials, which is still a reasonable low-order interpolation for plates and very simple to implement [21], in contrast with triangular elements which use higher order polynomials [21], such as the Argyris element [22]. The displacement field is approximate as:

$$u, v, w = \sum_{i=1}^{4} \boldsymbol{S}_i^{u,v,w} \boldsymbol{u_{e}}_i \tag{10}$$

where $\boldsymbol{u_{e}}_i$ contains the 6 degrees-of-freedom of the i^{th} node. The shape functions $\boldsymbol{S}_i^{u,v,w}$ are defined as:

$$\begin{aligned} \boldsymbol{S}_i^u &= \begin{bmatrix} L_i & 0 & 0 & 0 & 0 & 0 \end{bmatrix} \\ \boldsymbol{S}_i^v &= \begin{bmatrix} 0 & L_i & 0 & 0 & 0 & 0 \end{bmatrix} \\ \boldsymbol{S}_i^w &= \begin{bmatrix} 0 & 0 & H_i & H_i^x & H_i^y & H_i^{xy} \end{bmatrix} \end{aligned} \tag{11}$$

with L_i, H_i, H_i^x, H_i^y, H_i^{xy} calculated using natural coordinates [23, 24, 25]:

$$\begin{aligned} L_i &= \tfrac{1}{4}(1+\xi\xi_i)(1+\eta\eta_i) \\ H_i &= \tfrac{1}{16}(\xi+\xi_i)^2(\xi\xi_i-2)(\eta+\eta_i)^2(\eta\eta_i-2) \\ H_i^x &= -\tfrac{\ell_x}{32}\xi_i(\xi+\xi_i)^2(\xi\xi_i-1)(\eta+\eta_i)^2(\eta\eta_i-2) \\ H_i^y &= -\tfrac{\ell_y}{32}(\xi+\xi_i)^2(\xi\xi_i-2)\eta_i(\eta+\eta_i)^2(\eta\eta_i-1) \\ H_i^{xy} &= \tfrac{\ell_x\ell_y}{64}\xi_i(\xi+\xi_i)^2(\xi\xi_i-1)\eta_i(\eta+\eta_i)^2(\eta\eta_i-1) \end{aligned} \tag{12}$$

where ℓ_x, ℓ_y are respectively the finite element dimensions along x, y The values of ξ_i, η_i given in Eq. 13 were

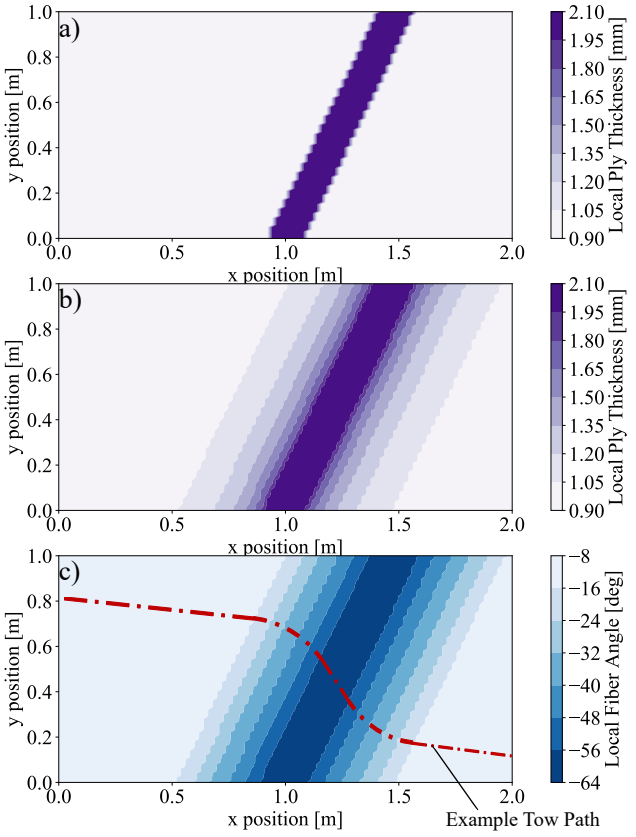

Figure 9: a): idealized stiffened ply thickness distribution. Plot b): ply thickness distribution with transition regions due to radius of curvature constraint. c): ply angle distribution with transition region due to radius of curvature constraints. Tows follow the angle distribution, as illustrated with the example tow path.

adopted for each of the four nodes.

$$\begin{array}{ccc} Node & \xi_i & \eta_i \\ 1 & -1 & -1 \\ 2 & +1 & -1 \\ 3 & +1 & +1 \\ 4 & -1 & +1 \end{array} \tag{13}$$

In the present study only rectangular elements were used, such that the natural coordinates can be defined simply as $\xi = 2x/\ell_x - 1, \eta = 2y/\ell_y - 1$. All required derivatives of $\boldsymbol{S}_i^{u,v,w}$ can then be calculated in terms of the natural coordinates using Eq. 14. All integrations over the finite element domains are performed numerically using standard Guass-quadrature and a mesh of 4×4 integration points per element.

$$\begin{aligned} \frac{\partial}{\partial x} &= \frac{\ell_x}{2}\frac{\partial}{\partial \xi} \\ \frac{\partial}{\partial y} &= \frac{\ell_y}{2}\frac{\partial}{\partial \eta} \end{aligned} \tag{14}$$

3.2. Linear buckling analysis

linear buckling behavior can be calculated applying the neutral equilibrium criterion [26]:

$$\delta^2 \Pi = 0 \tag{15}$$

where Π is the total potential energy functional. Replacing the expressions for the elastic energy and external work into Eq. 15, the following generalized eigenvalue problem can be derived [26]:

$$\boldsymbol{K_0} + \lambda \boldsymbol{K_{G0}} = 0 \tag{16}$$

where $\boldsymbol{K_0}$ is the global constitutive stiffness matrix of the system, and $\boldsymbol{K_{G0}}$ the geometric or initial stress stiffness matrix. Equation 17 gives the expression used to assemble $\boldsymbol{K_0}$ with the contribution of each plate finite element e of dimensions in x and y direction respectively given by ℓ_x and ℓ_y.

$$\boldsymbol{K_0} = \sum_{e=1}^{k} \frac{\ell_x \ell_y}{4} \iint_{\xi\eta} \boldsymbol{B_e}^T \boldsymbol{F} \boldsymbol{B_e} d\xi d\eta \tag{17}$$

In Eq. 17, $\boldsymbol{B_e}$ is directly obtained from the shape functions of Eq. 11 and the kinematic relations for plates, as given in Eq. 18. Since the BFS element has 6 degrees-of-freedom per node and 4 nodes per element, the shape of $\boldsymbol{B_e}$ is 24×6.

$$\boldsymbol{B_e}^T = \left[\frac{\partial \boldsymbol{S^u}}{\partial x}, \frac{\partial \boldsymbol{S^v}}{\partial y}, \frac{\partial \boldsymbol{S^u}}{\partial y} + \frac{\partial \boldsymbol{S^v}}{\partial x}, -\frac{\partial^2 \boldsymbol{S^w}}{\partial x^2}, -\frac{\partial^2 \boldsymbol{S^w}}{\partial y^2}, -2\frac{\partial^2 \boldsymbol{S^w}}{\partial x \partial y} \right] \tag{18}$$

Matrix $\boldsymbol{F}$ contains the constitutive stiffness for a plate obtained with classical laminated plate theory (CLPT):

$$\boldsymbol{F} = \begin{bmatrix} A_{11} & A_{12} & A_{16} & B_{11} & B_{12} & B_{16} \\ A_{12} & A_{22} & A_{26} & B_{12} & B_{22} & B_{26} \\ A_{16} & A_{26} & A_{66} & B_{16} & B_{26} & B_{66} \\ B_{11} & B_{12} & B_{16} & D_{11} & D_{12} & D_{16} \\ B_{12} & B_{22} & B_{26} & D_{12} & D_{22} & D_{26} \\ B_{16} & B_{26} & B_{66} & D_{16} & D_{26} & D_{66} \end{bmatrix} \tag{19}$$

where the calculation of A_{ij}, B_{ij}, D_{ij} can be found, for instance, in Jones [27] or Kassapoglou [15].

$$\boldsymbol{K_{G0}} = \sum_{e=1}^{k} \frac{\ell_x \ell_y}{4} \iint_{\xi\eta} \begin{bmatrix} \frac{\partial \boldsymbol{S^w}}{\partial x} \\ \frac{\partial \boldsymbol{S^w}}{\partial y} \end{bmatrix}^T \begin{bmatrix} N_{xx} & N_{xy} \\ N_{xy} & N_{yy} \end{bmatrix} \begin{bmatrix} \frac{\partial \boldsymbol{S^w}}{\partial x} \\ \frac{\partial \boldsymbol{S^w}}{\partial y} \end{bmatrix} d\xi d\eta \tag{20}$$

Note in Eq. 17 for $\boldsymbol{K_0}$ that $\boldsymbol{F}$ contains the constitutive terms that will be used to represent the stiffness variation of the proposed plate designs. In Eq. 20 for $\boldsymbol{K_{G0}}$ the membrane stress state given by N_{xx}, N_{yy} and N_{xy} will also depend on

the local stiffness properties. Therefore, during the numerical integration of $\boldsymbol{K_0}$ and $\boldsymbol{K_{G0}}$ one must know the local values of $\boldsymbol{F}(\xi,\eta)$ and $N_{xx}(\xi,\eta)$, $N_{yy}(\xi,\eta)$ and $N_{xy}(\xi,\eta)$, within each finite element. In the present study, the numerical integration is performed using a mesh of 4×4 integration points defined with standard Guass-quadrature rules.

4. Optimization through a genetic algorithm

Previous applications of genetic algorithms in the optimization of composites designs include laminate stacking sequence of several plates under buckling and strength constraints [8] and stiffened panels [28] and wingbox structures. For the latter, McIhagga et al. [29] compared different search schemes against genetic algorithms. Wan et al. [30] performed aeroelastic tailoring to minimize the wingbox skin weight. Arizono et al. [31] used a GA to find the minimum weight of a supersonic wingbox structure using static strength, local buckling, and minimum flutter speed as constraints. Castro et al. investigated: fast GA schemes with progressive mesh refinement to allow for more exploration of the design space [32]; the effect of GA parameters [33]; comparison with gradient-based methods [34]; and different parameterization schemes [35]. Jin et al. [36] used parallel GA for large wingbox optimizations. More recently, Liguori et al. [37] applied GA in the optimization of a variable-angle tow wingbox construction considering post-buckling constraints.

The optimization of the panels herein addressed is a significant nonlinear problem made exponentially more complex by the amount of variables that become involved as the ply count increases. However, the vector descriptions for plies and laminates, given in Equation 2 and Equation 3 respectively, led to a representation that could well be used as the genetic data in a genetic algorithm. The present genetic algorithm was written using the Distributed Evolutionary Algorithms in Python (DEAP) module [38]. The workings of the algorithm are illustrated in Figure 10.

It should be noted that the previously mentioned constraints for the variables describing a ply are maintained throughout all steps of the process. Randomization, mutation and crossover of individual ply variables thus become all constrained operations. The same goes for randomization of full plies, or full laminates.

Some special operations are used during mutation and mating. Two types of crossover and three types of mutation are utilized to try and maximize the improvement of the genetic data from generation to generation.

For mating the more conventional variable crossover from one ply to another is described in Equation 21. A random variable in one ply in a laminate is replaced by that same variable from a ply in another laminate.

$$\begin{aligned}
&\boldsymbol{P_{i,n}} = [\theta_{0_{i,n}}, \theta_{1_{i,n}}, w_{s_{i,n}}, \phi_{s_{i,n}}, x_{s_{i,n}}] \\
&+ \\
&\boldsymbol{P_{j,m}} = [\theta_{0_{j,m}}, \theta_{1_{j,m}}, w_{s_{j,m}}, \phi_{s_{j,m}}, x_{s_{j,m}}] \\
&\Downarrow \quad \text{variable crossover} \\
&\boldsymbol{P_{i,n}} = [\theta_{0_{i,n}}, \theta_{1_{i,n}}, w_{s_{j,m}}, \phi_{s_{i,n}}, x_{s_{i,n}}]
\end{aligned} \tag{21}$$

Less conventionally, a full ply crossover of one ply from a laminate, fully replacing a ply in another laminate, can also be performed, as per Equation 22.

$$\begin{aligned}
&\boldsymbol{L_i} = [\boldsymbol{P_{i,1}}, \boldsymbol{P_{i,2}}, \boldsymbol{P_{i,3}}, \boldsymbol{P_{i,4}}, \boldsymbol{P_{i,5}}] \\
&+ \\
&\boldsymbol{L_j} = [\boldsymbol{P_{j,1}}, \boldsymbol{P_{j,2}}, \boldsymbol{P_{j,3}}, \boldsymbol{P_{j,4}}, \boldsymbol{P_{j,5}}] \\
&\Downarrow \quad \text{ply crossover} \\
&\boldsymbol{L_i} = [\boldsymbol{P_{i,1}}, \boldsymbol{P_{i,2}}, \boldsymbol{P_{j,5}}, \boldsymbol{P_{i,4}}, \boldsymbol{P_{i,5}}]
\end{aligned} \tag{22}$$

Variable and ply mutation work the same as they do for ply crossover, but the single variable/ply is instead replaced by a randomly generated variable/ply. Finally, full randomization randomly generates an entirely new laminate to replace an old laminate. This operation is introduced to ensure a steady stream of genetic data from throughout the entire design space.

The algorithm starts out with a randomly generated initial population of n individuals. These get tested for their buckling strength and ranked in performance according to a fitness equation. The best $0.5n$ laminates immediately continue to the next generation. The genetic data of the entire population is subsequently mixed through mating and mutation to create $0.5n$ new laminates. These new laminates get evaluated for buckling performance, ranked, and the cycle continues.

After m generations laminates remaining should in theory show significantly better buckling performance than the laminates of the initial random population. The best panel in the final generation is output as the optimized panel.

5. Benchmarking against Existing Literature

To prove that the methodology described above is capable of generating better performing laminates than conventional straight fiber laminates, a benchmark optimization problem is set up.

5.1. Benchmark Case Setup

The benchmark case is taken from the results of Le Riche and Haftka [8], where straight fiber laminates were optimized for buckling performance under bi-axial compression through a genetic algorithm. The stacking sequence of the optimal 64 ply laminate used is as follows: $(90_{10}, \pm45_2, 90_2, \pm45_3, 90_2, \pm45_4)_s$.

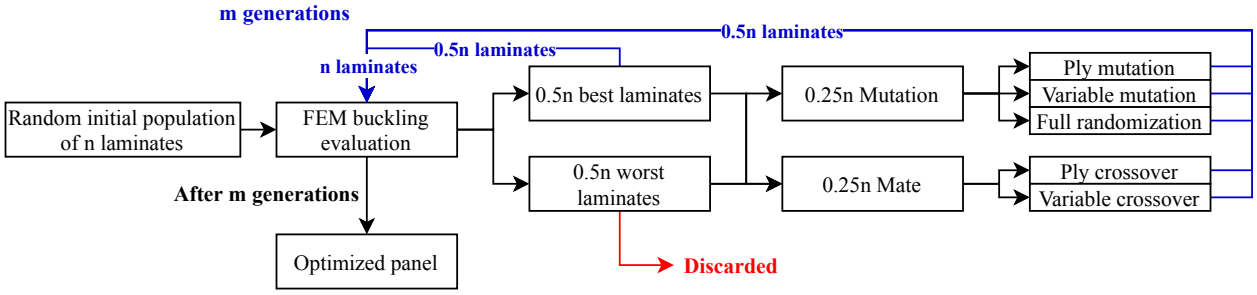

Figure 10: Flow chart of the genetic algorithm.

The geometry of the laminate is a simple plate, of which $a = 0.508$ m and $b = 0.254$ m. The bi-axial load case is illustrated in Figure 11. The load factor, λ (N/m), is applied to both the x and y directions [8]. The plate is simply supported on all sides.

The material properties are those of graphite-epoxy carbon reinforced polymer. With $E_1 = 127.59$ GPa, $E_2 = 13.03$ GPa, $\nu_{12} = 0.3$, $G_{12} = 6.41$ GPa. The tow thickness is $t_p = 0.127$ mm.

In the BFS finite element used in the present study, the λ achieved by the reference panel is 6.96×10^5 N/m. The load factor achieved in [8], converted from imperial units, was 6.96×10^5 N/m, which shows correspondence to the method employed in [8] to within a 1% error, verifying the BFS finite element herein implemented for calculating the buckling constraint.

The performance comparison against the benchmark is determined by dividing its buckling failure load, λ, by the total panel volume. The overlaps of the VAT stiffened panel add volume, and thus weight. Therefore, the volume-normalized buckling load becomes a fairer way to compare the optimal straight-fiber plate against the VAT overlap-stiffened panels with regards to their buckling performance.

This comparison serves as a proof of concept. Once it is proven that the VAT overlap-stiffened panel can provide a better volume-normalized buckling performance than a straight fiber panel, there is a good probability that one is able to design a VAT overlap-stiffened panel to be lighter than a straight fiber panel, while constrained by a given design load.

6. Overlap-stiffened panel optimizations

The genetic algorithm is set to the same geometric and material values as those of the reference panel. Additionally, the minimum radius of curvature R_0 is set to 450 mm for the AFP panel and to 50 mm for the CTS panel.

The plies within the 64 ply laminates are generated and optimized with the genetic algorithm as described in the methodology. The population size n is set to 100, and the number of generations m is set to 150. With these settings the improvement of the laminates generally stagnates at around the 140th generation in test runs

From generation to generation the better laminates are selected according to the fitness function in Equation 23. In this way, the genetic algorithm works towards optimizing the overlap-stiffened panels aiming at a maximum volume-normalized buckling load.

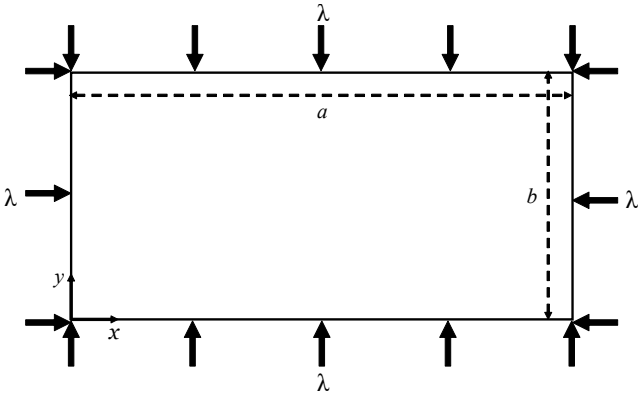

Figure 11: Bi-axial load case used to determine the buckling strength of the laminates.

[8]

$$max(\frac{\lambda}{\text{panel volume}}) \tag{23}$$

The way the design space is set up and constrained is explained in the methodology. In the ply generation algorithm all angle values θ_0, θ_1, and Φ_s are set to only take on integer degree values within the given constraints. The values of w_s and x_s can only be one out of 20 and 100 discretized values, respectively. Even smaller levels of discretization would most likely not make a meaningful difference in the achievable level of buckling load, while significantly increasing the size of the design space.

Taking into account all aforementioned ply generation constraints, the present optimization problem leads to an approximate design space having $8 \cdot 10^{10}$ possible 64 ply laminate individuals, with there being well over $1 \cdot 10^9$ different individual ply combinations. The unconstrained design space is comprised of approximately $1.6 \cdot 10^{11}$ different laminates.

The relatively simple parameterization of the laminates and plies herein proposed serves to narrow the design space

significantly, as it could be many orders of magnitude larger with a more complex parameterization method.

With $n = 150$ and $m = 100$, and making the approximation that every mutation or crossover will result in a unique untested laminate, the algorithm will at most test 7600 unique laminates per run. As a result, the algorithm is almost guaranteed to end up in a highly local optimum. A more sophisticated algorithm will be required to approach global optima, or to be able to cycle through a larger part of the design space in a single run. However, for the purposes of the present study, the current algorithm is sufficient to show a proof viability of the VAT overlap-stiffened design method.

7. Results

The results of the reference panel, the optimized AFP panel, and the optimized CST panel are displayed in Table 1.

The AFP panel resulted in a 154% improvement in the volume-normalized buckling load over the reference panel, followed by the CST panel with 111% improvement. These results are not unexpected. The reference panel and the AFP and CTS panels all have the same amount of layers, with the AFP and CTS panels both being able to achieve a higher thickness due to the overlapping. The increase in thickness will generally always result in a panel with a better volume-normalized buckling load.

The final thickness distributions of the AFP and the CTS panel are illustrated in Figure 12 and Figure 13, respectively; where both show a relatively similar trend, with the thickness increasing towards the center of the panel. The AFP panel achieves a higher maximum and average overall thickness compared to the CTS panel. The difference in thickness distributions is likely a direct result of the way in which the minimum radius of curvature setting interacts with the thickness distribution of the plies. The AFP panel's R_0 is almost as big as the ply, meaning that the thickness transition regions accompanying the ply stiffeners will usually cause an increase in thickness over a majority of the ply area.

The CTS panel, on the other hand, has a relatively small R_0 setting, thus creating small thickness transition regions. The thickness increase will, as a result, remain more localized to the actual idealized stiffener location, resulting in plies with a thinner average thickness.

Consequently, the AFP panel result is likely to be thicker than the CTS panel result, as confirmed by the present results.

Finally, it should be noted that the present results should not be taken as the maximum volume-normalized buckling values that can be achieved by the present design parameterization, considering that the genetic algorithm does not guarantee a global optimum. The reader should interpret the values in Table 1 as the best results of multiple runs of the genetic algorithm for each panel design.

8. Conclusions

Variable-angle tow overlap-stiffened panels were presented as a new design possibility taking advantage of tow overlaps in automated fiber placement (AFP) and inherent steering-thickness variation in continuous tow shearing (CTS). In the design and optimization examples herein demonstrated, manufacturability constraints were included and a design parameterization using a reduced number of variables was proposed, whereby only 5 variables are necessary per ply containing one straight overlap-stiffener.

A method for testing and optimizing such overlap-stiffened panels for buckling performance was developed, and subsequently applied to the optimization of an AFP and a CTS overlap-stiffened panel, aiming at a maximized specific buckling performance. The new overlap-stiffened design outperformed the straight-fiber design for the study case herein investigated.

The minimum radius of curvature manufacturing constraint was successfully satisfied in the ply generation algorithm by connecting two different assigned thicknesses by circular arcs, of which the radius of curvature will always exceed the minimum allowable radius of curvature.

A genetic algorithm was written for optimization of the volume-normalized buckling loads of both AFP and CTS panels simulating overlap-stiffened 64-ply designs. These panels were benchmarked against a straight design also with 64 plies, optimized for biaxially compressive loading conditions. The AFP and CTS panels are capable of outperforming the reference panel on the volume-normalized buckling load by at least 154% and 111%, respectively. The AFP panel was 60% heavier than the reference panel, and the CTS panel was 50% heavier.

In conclusion, a solid foundation was laid out for the design of the overlap-stiffened plies, with the method showing a large potential in being able to improve the buckling performance of composite panels.

8.1. Future Studies

Now that the design of overlap-stiffened panels have been shown their potential for maximizing volume-normalized buckling loads, a logical next step is to modify the optimization to design a lighter panel for a given design load. This could be achieved by making the number of plies in the overlap-stiffened laminate variable.

Additionally, the method could be modified with countless different design parameters that would suit different geometries and desired design assumptions. Multiple stiffeners per ply, curved stiffeners, a mix of normal straight-fiber plies and overlap-stiffened plies, stiffeners which vary in thickness along their length, and incorporating the same stiffener in every single ply to create one big laminate stiffener; are all examples of possible designs to be explored.

Acknowledgements

The authors thank the Delft University of Technology Aerospace Engineering Honours Program Bachelor for pro-

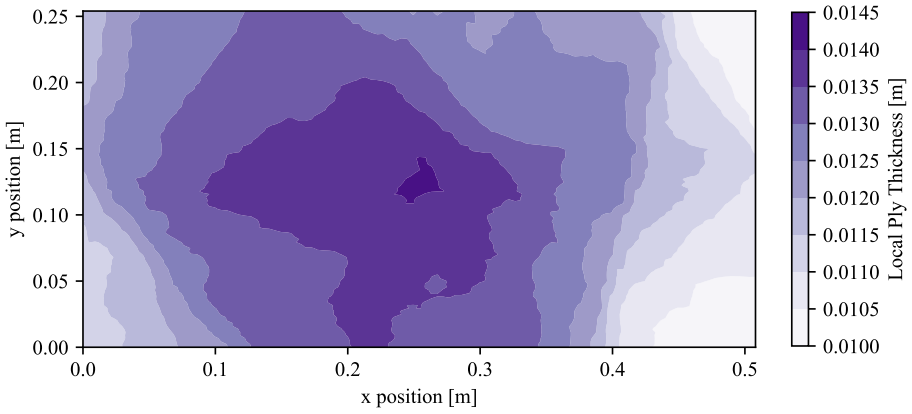

Figure 12: Final thickness distribution of the optimized VAT overlap-stiffened panel using AFP with $R_0 = 450$ mm.

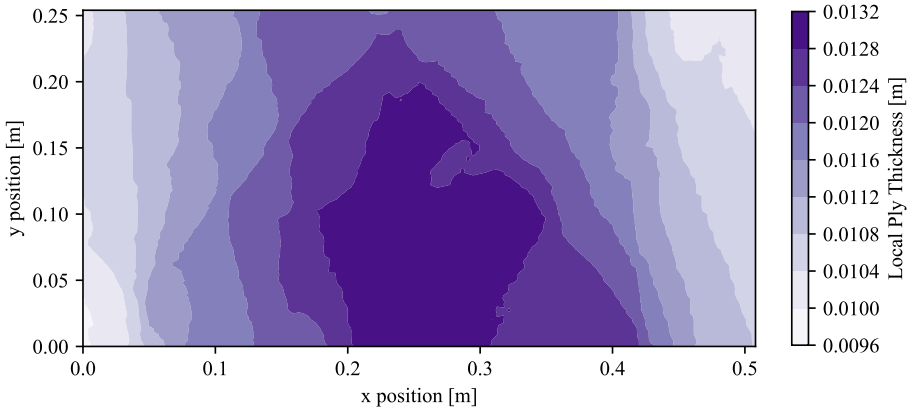

Figure 13: Final thickness distribution of the optimized VAT overlap-stiffened panel using CTS with $R_0 = 50$ mm.

viding the opportunity and the support for them to work together on, and complete this piece of research.

CRediT authorship contribution statement

Raphael Ummels: Methodology, formal analysis, investigation, validation, software, writing - original draft preparation, writing - editing. **Saullo G. P. Castro:** Conceptual-

Table 1
Final result comparison of buckling performance of the reference panel and the VAT stiffened panels.

Panel	λ $[N/m]$	volume $[m^3]$	volume-normalized λ $[N/m^3]$	Improvement over reference panel [%]
Reference Panel [8]	6.96e5	1.01e-3	6.63e8	0
AFP Panel	23.5e5	1.63e-3	16.9e8	154
CST Panel	21.4e5	1.53e-3	14.0e8	111

ization, investigation, supervision, software, writing - original draft preparation, writing - editing.

References

[1] Z. Gurdal, R. Olmedo, In-plane response of laminates with spatially varying fiber orientations - Variable stiffness concept, AIAA Journal 31 (4) (1993) 751–758. doi:10.2514/3.11613.

[2] A. W. Blom, Structural performance of fiber-placed, variable-stiffness composite conical and cylindrical shells, Phd in aerospace engineering, Delft University of Technology (2010).

[3] A. W. Blom, P. B. Stickler, Z. Gürdal, Optimization of a composite cylinder under bending by tailoring stiffness properties in circumferential direction, Composites Part B: Engineering 41 (2) (2010) 157 – 165. doi:https://doi.org/10.1016/j.compositesb.2009.10.004.

[4] Z. Wang, J. H. S. Almeida Jr., L. St-Pierre, Z. Wang, S. G. P. Castro, Reliability-based buckling optimization with an accelerated Kriging metamodel for filament-wound variable angle tow composite cylinders, Composite Structures (2020) 112821doi:10.1016/j.compstruct.2020.112821.
URL https://linkinghub.elsevier.com/retrieve/pii/S0263822320327471

[5] B. C. Kim, K. Potter, P. M. Weaver, Continuous tow shearing for manufacturing variable angle tow composites, Composites Part A: Applied Science and Manufacturing 43 (8) (2012) 1347–1356. doi:10.1016/J.COMPOSITESA.2012.02.024.

[6] S. G. Castro, M. V. Donadon, T. A. Guimarães, ES-PIM applied to buckling of variable angle tow laminates, Composite Structures 209 (2019) 67 – 78. doi:https://doi.org/10.1016/j.compstruct.2018.10.058.

[7] G. Clancy, D. Peeters, V. Oliveri, D. Jones, R. M. O'Higgins, P. M. Weaver, A study of the influence of processing parameters on steering of carbon Fibre/PEEK tapes using laser-assisted tape placement, Composites Part B: Engineering 163 (2019) 243–251. doi:10.1016/j.compositesb.2018.11.033.

[8] R. L. Riche, R. T. Haftka, Optimization of laminate stacking sequence for buckling load maximization by genetic algorithm., AIAA Journal 31 (1993) 951–956.

[9] C. S. Lopes, Z. Gürdal, P. P. Camanho, Variable-stiffness composite panels: Buckling and first-ply failure improvements over straight-fibre laminates, Comput. Struct. 86(9) (2008). doi:https://doi.org/10.1016/j.compstruc.2007.04.016.

[10] L. Vertonghen, Semi-Analytical Buckling and Optimisation of Variable Stiffness, Variable Thickness Laminates, Ph.D. thesis, Delft University of Technology (2019).
URL https://repository.tudelft.nl/islandora/object/uuid%3Ac8fa3202-dac8-4246-8ff2-eb08f3ac008a

[11] L. Vertonghen, S. G. P. Castro, Modelling of fibre steered plates with coupled thickness variation from overlapping continuous tows (2020). doi:10.31224/OSF.IO/9BJY6.
URL https://engrxiv.org/9bjy6/

[12] R. M. J. Groh, P. M. Weaver, Buckling analysis of variable angle tow, variable thickness panels with transverse shear effects, Composite Structures 107 (2014) 482–493. doi:10.1016/j.compstruct.2013.08.025.

[13] C. Mittelstedt, Closed-form analysis of the buckling loads of uniaxially loaded blade-stringer-stiffened composite plates considering periodic boundary conditions, Thin-Walled Structures 45 (4) (2007) 371–382. doi:10.1016/j.tws.2007.04.005.
URL https://linkinghub.elsevier.com/retrieve/pii/S0263823107000870

[14] M. Beerhorst, M. Seibel, C. Mittelstedt, Closed-form Approximate Solution for the Postbuckling Behavior of Orthotropic Shallow Shells Under Axial Compression, 2011, pp. 103–124. doi:10.1007/978-3-642-21855-2_9.
URL http://link.springer.com/10.1007/978-3-642-21855-2_9

[15] C. Kassapoglou, Design and Analysis of Composite Structures, 2nd Edition, John Wiley Sons Ltd, Oxford, UK, 2013. doi:10.1002/9781118536933.
URL http://doi.wiley.com/10.1002/9781118536933

[16] S. G. Castro, C. Mittelstedt, F. A. Monteiro, R. Degenhardt, G. Ziegmann, Evaluation of non-linear buckling loads of geometrically imperfect composite cylinders and cones with the Ritz method, Composite Structures 122 (2015) 284–299. doi:10.1016/j.compstruct.2014.11.050.

[17] S. G. Castro, C. Mittelstedt, F. A. Monteiro, M. A. Arbelo, R. Degenhardt, G. Ziegmann, A semi-analytical approach for linear and non-linear analysis of unstiffened laminated composite cylinders and cones under axial, torsion and pressure loads, Thin-Walled Structures 90 (2015) 61–73. doi:10.1016/j.tws.2015.01.002.

[18] F. K. Bogner, R. L. Fox, L. A. Schmit Jr., The generation of inter-element-compatible stiffness and mass matrices by the use of interpolation formulas, in: Matrix Methods in Structural Mechanics, Air-Force Inst. of Tech., Wright Patterson AF Base, Cleveland, Ohio, 1966, pp. 395–444.
URL http://contrails.iit.edu/reports/8569

[19] O. C. Zienkiewicz, R. L. Taylor, The Finite Element Method Volume 2: Solid Mechanics, fifth edit Edition, 2000.

[20] S. Castro, E. Jansen, Displacement-based formulation of Koiter's method: Application to multi-modal post-buckling finite element analysis of plates, Thin-Walled Structures (2020) 107217doi:10.1016/j.tws.2020.107217.
URL https://linkinghub.elsevier.com/retrieve/pii/S0263823120310892

[21] E. Burman, M. G. Larson, P. Hansbo, Cut Bogner-Fox-Schmit Elements for Plates (nov 2019). arXiv:1911.00239.
URL http://arxiv.org/abs/1911.00239

[22] J. H. Argyris, I. Fried, D. W. Scharpf, The TUBA Family of Plate Elements for the Matrix Displacement Method, The Aeronautical Journal 72 (692) (1968) 701–709. doi:10.1017/S000192400008489X.
URL https://www.cambridge.org/core/product/identifier/S000192400008489X/type/journal{_}article

[23] O. O. Ochoa, J. N. Reddy, Finite Element Analysis of Composite Laminates, Springer, Dordrecht, 1992, pp. 37–109. doi:10.1007/978-94-015-7995-7_3.
URL http://link.springer.com/10.1007/978-94-015-7995-7{_}3

[24] D. Q. Tsunematsu, The aeroelastic behavior of laminated composite panels undergoing progressive damage in supersonic flow, Thesis of doctor of science, Instituto Tecnológico de Aeronáutica (2019).

[25] D. Q. Tsunematsu, M. V. Donadon, Aeroelastic behavior of composite panels undergoing progressive damage, Composite Structures 210 (2019) 458–472. doi:10.1016/J.COMPSTRUCT.2018.11.065.
URL https://www.sciencedirect.com/science/article/pii/S0263822318314508{#}b0110

[26] S. G. P. Castro, C. Mittelstedt, F. A. Monteiro, M. A. Arbelo, G. Ziegmann, R. Degenhardt, Linear buckling predictions of unstiffened laminated composite cylinders and cones under various loading and boundary conditions using semi-analytical models, Composite Structures 118 (2014) 303 – 315. doi:https://doi.org/10.1016/j.compstruct.2014.07.037.

[27] R. M. Jones, Mechanics of Composite Materials Jones 1999, 1999. doi:10.1007/BF00611782.

[28] S. Nagendra, D. Jestin, Z. Gürdal, R. T. Haftka, L. T. Watson, Improved genetic algorithm for the design of stiffened composite panels, Computers & Structures 58 (3) (1996) 543–555.

[29] M. McIlhagga, P. Husbands, R. Ives, A comparison of search techniques on a wing-box optimisation problem, in: Lecture Notes in Computer Science (including subseries Lecture Notes in Artificial Intelligence and Lecture Notes in Bioinformatics), Vol. 1141, Springer Verlag, 1996, pp. 614–623. doi:10.1007/3-540-61723-X_1025.
URL https://link.springer.com/chapter/10.1007/3-540-61723-X_1025

[30] Z. Wan, C. Yang, Z. Li, Application of hybrid genetic algorithm in aeroelastic multidisciplinary optimization, Beijing Hangkong Hangtian Daxue Xuebao/Journal of Beijing University of Aeronautics and Astronautics (2004).

[31] H. Arizono, K. Isogai, Application of genetic algorithm for aeroelastic tailoring of a cranked-arrow wing, Journal of Aircraft (2005). doi:10.2514/1.392.

[32] S. G. Castro, J. A. Hernandes, E. Lucena Neto, Composite wing optimization with progressive mesh refinement, in: 20th International Congress of Mechanical Engineering, Gramado, RS, Brazil, 2009.
URL https://www.researchgate.net/publication/233406731_Composite_wing_optimization_with_proggressive_mesh_refinement

[33] S. G. Castro, J. A. Hernandes, F. L. d. S. Bussamra, W. M. Ponciano, Finding optimal genetic algorithm parameters for a composite wing optimization, in: 11th Pan-American Congress of Applied Mechanics (PACAM), Foz do Iguaçu, PR, Brazil, 2010.
URL https://www.researchgate.net/publication/233406886_Finding_optimal_genetic_algorithm_parameters_for_a_composite_wing_optimization

[34] S. G. Castro, T. A. Guimarães, J. A. Hernandes, Composite optimization performance comparison between GENESIS (R) BIGDOT and ModeFrontier (R) MOGAII algorithms, in: VI NATIONAL CONGRESS OF MECHANICAL ENGINEERING (CONEM), Campina Grande – Paraíba – Brazil, 2010.
URL https://www.researchgate.net/publication/233406745_Composite_optimization_performance_comparison_between_GENESIS_R_BIGDOT_and_ModeFrontier_R_MOGAII_algorithms

[35] S. G. Castro, T. A. Guimarães, J. A. Hernandes, Comparison of free stacking sequence approach versus a predefined 0/+45/-45/90 sequence in a typical aircraft wing optimization, in: 2nd International Conference on Engineering Optimization (ENGOPT), Lisbon, Portugal, 2010.
URL https://www.researchgate.net/publication/233406751_Comparison_of_free_stacking_sequence_approach_versus_a_predefined_045-4590_sequence_in_a_typical_aircraft_wing_optimization

[36] P. Jin, B. Song, X. Zhong, Structure optimization of large composite wing box with parallel genetic algorithm, Journal of Aircraft 48 (6) (2011) 2145–2148. doi:10.2514/1.C031493.
URL https://arc.aiaa.org/doi/abs/10.2514/1.C031493

[37] F. S. Liguori, G. Zucco, A. Madeo, D. Magisano, L. Leonetti, G. Garcea, P. M. Weaver, Postbuckling optimisation of a variable angle tow composite wingbox using a multi-modal Koiter approach, Thin-Walled Structures 138 (2019) 183–198. doi:10.1016/j.tws.2019.01.035.

[38] F.-A. Fortin, F.-M. De Rainville, M.-A. Gardner, M. Parizeau, C. Gagné, DEAP: Evolutionary algorithms made easy, Journal of Machine Learning Research 13 (2012) 2171–2175.